Intense laser dissociation of D_2^+: From experiment to theory

V. Serov,* A. Keller, and O. Atabek
Laboratoire de Photophysique Moléculaire du CNRS, Université de Paris-Sud, 91405 Orsay, France

H. Figger and D. Pavicic
Max-Planck-Institut fur Quantenoptik, Hans-Kopfermann-Strasse 1, D-85748 Garching, Germany
(Received 2 June 2005; published 20 September 2005)

Accurate angularly resolved photodissociation spectra are recorded using electric discharge for preparing the molecular ions, under intense (about 10^{14} W/cm^2), short (about 140 fs) laser pulse excitation at 748 nm wavelength. Such experiments are particularly convenient for the interpretation level of theoretical models that neglects ionization-dissociation competition. Abel transformation relates the center-of-mass dissociation probability to the laboratory frame observations. A spatial field average over the laser focus area, together with some statistics on molecular initial rovibrational states, yields to fragments kinetic and angular distributions that are directly comparable to experimental data. Due to small-angle Coulomb explosion, not explicitly taken into account by the model, the theory-versus-experiment confrontation can be quantitatively conducted only for angles exceeding $\pi/7$. Very good agreement is obtained for spectra including both single- and two-photon processes that are enhanced at such high laser intensities. The level of accuracy which is reached advocates both for the correct arrangement of the different steps of the theory and for the basic mechanisms (namely, bond softening and vibrational trapping) that are used as interpretative tools.

DOI: 10.1103/PhysRevA.72.033413 PACS number(s): 42.50.Hz, 33.80.Gj

I. INTRODUCTION

During the last decade numerous observations have been made in the intense laser above-threshold multiphoton ionization and dissociation of H_2^+ and its isotope D_2^+, addressing not only fragmentation rates, but also angular distributions [1–7]. Such observations have received a comprehensive frame in terms of some basic mechanisms evidenced through the light-induced adiabatic potentials describing the dressed states of the molecule-plus-field system [8]. More explicitly, bond softening [4,9] and its opposite vibrational trapping [10,11] in the visible-UV frequency range, with their counterparts, barrier suppression [12], and dynamical dissociation quenching in the IR regime [13], have been successfully used, not only as interpretative tools but also for guiding control scenarios. Despite all this knowledge, only very few attempts have been made for a thorough quantitative theory-versus-experiment comparison [14]. This is presumably due to the difficulty for the models to include the ionization-dissociation competition and the Coulomb explosion, on the one hand, and for the experimental works to perform careful investigations of rovibrational populations and reach high accuracy for momentum and angular resolution, on the other hand. It is only very recently that ion beam experiments, where H_2^+ or D_2^+ ions are produced in an electric plasma discharge, have been conducted with a high degree of angular resolution [15]. As opposite to previous studies, using a laser prepulse for ionizing the neutral molecule H_2 or D_2 [1,3,8], the electric discharge disentangles ionization and dissociation processes and the resolution is enough for identifying fragments originating from different initial vibrational states of H_2^+ or D_2^+ [15,16].

This work, at least concerning its theoretical background, is a continuation of Ref. [14], as applied to the intense field photodissociation spectra of D_2^+. But the laser peak intensities (about 10^{14} W/cm^2) are such that above-threshold dissociation (ATD) and Coulomb explosion processes are significantly enhanced when compared with the observations of Ref. [14] on H_2^+. The emphasis is put on kinetic energy spectra and angular distributions originating from net two-photon absorptions. Our model still does not account for the second ionization of the D_2^+ ion followed by its Coulomb explosion. But as will be evidenced hereafter, the dissociation of fragments moderately aligned with the linearly polarized laser is accurately calculated, as the Coulomb explosion requires intense radiative coupling and has, as expected, noticeable effect only on those fragments that are strongly aligned [15]. The paper is organized as follows: Section II describes the experimental setup. Section III gives, for the sake of completeness and self-consistency, a brief summary of the main theoretical features. Section IV is devoted to the results: kinetic energy and angular distributions of the fragments, with some comparisons between H_2^+ and D_2^+.

II. EXPERIMENTAL SETUP

Differing from almost all preceding experiments, D_2^+ is investigated here in an ionic beam. To that aim, D_2^+ ions are formed in a hollow-cathode electric discharge of the duoplasmatron type through D_2 gas. The ions are extracted from this source and accelerated to 11.1 keV corresponding to a velocity of $v \simeq 10^6$ m s^{-1}. The ion beam, consisting so far of many different ions, after some geometric formation passes a mass selecting sector magnetic field so that a pure beam of D_2^+ survives behind it, which is then collimated by two slits at a distance of 80 cm to a thin rectangular beam of 200

*Electronic address: vassili.serov@ppm.u-psud.fr

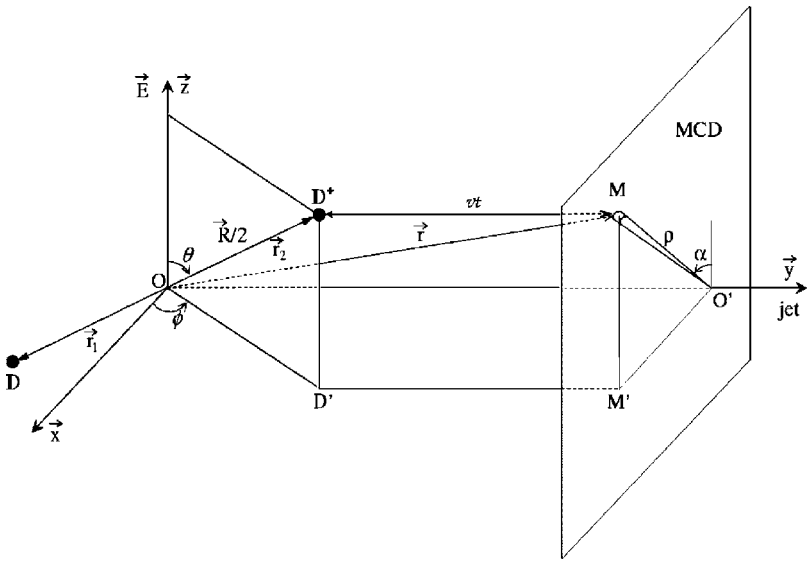

FIG. 1. The D_2^+ photodissociation experiment based on the ionization of D_2 using a discharge source.

$\times 20\ \mu m^2$ size. The intention of this stringent collimation is to reduce the intensity volume effect of the pulsed laser beam as well as to increase the spatial resolution of the fragments D on the two-dimensional detector. By an additional electric field the fragmental ions D^+ as well as the surviving parent ions D_2^+ can bent away from the fragmental neutrals D which then can be solely measured. The laser has a pulse length of 140 fs and a repetition rate of 1 kHz. Focused by a 30-mm lens, it crosses the ionic beam at a right angle after a second slit. The detector being positioned at a distance of $d=80$ cm from the laser focal point consists of an amplifying multichannel plate connected to a phosphor-covered plate to detect the electron bunches by their light flashes which are then read out by a charge-coupled-device (CCD) camera system whose output is fed into a PC. The energetic resolution of this two-dimensional detector decreases from the inner region to the outer part. It is around 10 meV. The geometrical arrangement is illustrated in Fig. 1. The response of the detector is linear in the momentum k_ρ of the fragment—i.e., the fragment velocity. The quantity which is measured is precisely this momentum k_ρ of the neutral atom D as recorded on a given pixel M (labeled by its polar coordinates ρ, α) of the CCD camera. Actually, as the beam velocity (i.e., the velocity of the center of mass G of D_2^+) is much larger than the recoiling D and D^+ fragment relative velocity, one can assume that atom D reaches the MCD (multichannel detector) plane at the same time t as G, given by $t=D/v$. Note that, at $t=0$, G is positioned at point O in Fig. 1. From the relation $\rho \simeq k_\rho t/m$, one gets

$$k_\rho = \frac{mv}{D}\rho, \tag{1}$$

where m is the mass of the D atom. As for the momentum k of the recoiling fragments in the center-of-mass frame—i.e., $k \simeq mR/2t$ (R meaning the interfragment distance)—one obtains

$$k = \frac{mv}{D}\frac{R}{2}. \tag{2}$$

Finally, the relation between the angles θ and α positioning the D atom in the center-of-mass and detector frames is merely obtained from the equality $R/2 \cos\theta = \rho \cos\alpha$ and referring to Eqs. (1) and (2):

$$\cos\theta = \frac{k_\rho}{k}\cos\alpha. \tag{3}$$

III. THEORY

A detailed description of the theory has been provided in Ref. [14]. For this paper to be self-consistent, we are giving, hereafter, some basic features of the model, putting the emphasis on the way to relate the dissociation probability calculated in the molecular frame to the signal recorded on the CCD camera. Within a classical view, in the center-of-mass frame and in the asymptotic region, fragments with a given momentum k are distributed on a sphere of radius $R_k(t) \simeq kt/m$ centered at G. As time goes on, the sphere is translated with the velocity v of G, and its radius increases, until it reaches and goes through the detector plane. The recorded signal is nothing but the sum of the projections of all such spheres (one per k) on the CCD camera. This is precisely the transformation that has to be worked out. The starting point is the number dN of D atoms detected at point $M(\rho, \alpha)$ flowing through unit surface dS:

$$\frac{dN}{dS} = \int_0^\infty \boldsymbol{j}(t)\cdot\boldsymbol{u}_y(t)\mathrm{d}t, \tag{4}$$

where $\boldsymbol{u}_y$ is the unit vector orthogonal to the detector plane and the current density vector is given by

$$\boldsymbol{j}(t) = \frac{1}{m}\int \mathrm{d}\boldsymbol{r}_2\ \mathrm{Im}[\Psi^*(\boldsymbol{R},\boldsymbol{R_G};t)\boldsymbol{\nabla}_{\boldsymbol{r}_1}\Psi(\boldsymbol{R},\boldsymbol{R_G};t)], \tag{5}$$

where $\Psi(\boldsymbol{R},\boldsymbol{R_G};t)$ is the overall wave packet describing the combined molecular internal $\boldsymbol{R}$ and center-of-mass $\boldsymbol{R_G}$ motions. In terms of the vectors $\boldsymbol{r}_1$ and $\boldsymbol{r}_2$ positioning the neutral atom D and its ion D^+ in the laboratory frame, one has $\boldsymbol{R}=\boldsymbol{r}_1-\boldsymbol{r}_2$ and $\boldsymbol{R_G}=(\boldsymbol{r}_1+\boldsymbol{r}_2)/2$. The integration over $\boldsymbol{r}_2$ accounts for D^+ ions that have not been detected in the experi-

ment. "Im" stands for the imaginary part. Separating the center-of-mass motion which is further described within the semiclassical approximation and referring to a (asymptotically valid) purely radial motion for $\boldsymbol{R}$, Eq. (5) is recast in an easily interpretable form

$$\boldsymbol{j}(t) = \frac{1}{mR^2}\mathrm{Im}\left[\Phi^*(\boldsymbol{R};t)\frac{\partial}{\partial R}\Phi(\boldsymbol{R};t)\boldsymbol{u_R} + imv|\Phi(\boldsymbol{R};t)|^2\boldsymbol{u_y}\right]\Bigg|_{\boldsymbol{R}=2\boldsymbol{r}_1-2vt\boldsymbol{u_y}}, \tag{6}$$

where $\Phi(\boldsymbol{R};t)$ is the wave packet calculated by solving the time-dependent Schrödinger equation in the molecular frame involving the ground $^2\Sigma_g^+$ and the first excited $^2\Sigma_u^+$ Born-Oppenheimer (BO) electronic states and correlated to an initial state $\Phi_{g,v,N,M_N}(\boldsymbol{R};t)$ with well-defined quantum labels: g for the electronic $^2\Sigma_g^+$ and v, N, and M_N for the vibrational and rotational quantum numbers. $\boldsymbol{u_R}=\boldsymbol{R}/R$ is the unit vector along the $\boldsymbol{R}$ direction.

The first term in Eq. (6) depicts the radial current density in the center-of-mass frame, whereas the second term represents an additional contribution to the current density in terms of a density of particles $|\Phi(\boldsymbol{R};t)|^2/R^2$ moving at the velocity v. This interpretation completes the classical picture provided in the introduction of Sec. III. In Eq. (4), we are actually interested only by the asymptotic part of the current density, with the remarkable result that the probabilities of observing $\boldsymbol{R}$ or $\boldsymbol{k}$ in a given direction (characterized by the polar angles θ and ϕ) are identical [14,17]. Implementing this property into Eq. (6)—i.e., replacing $\Phi(\boldsymbol{R};t)$ with its asymptotic form given in terms of its Fourier transform $\hat{\Phi}$—one finally obtains

$$\boldsymbol{j}(t) = \frac{m}{2Rt^2}\left[\boldsymbol{u_R}+\frac{2vt}{R}\boldsymbol{u_y}\right]\left|\hat{\Phi}\left(\frac{mR}{2t},\theta,\phi\right)\right|^2\Bigg|_{\boldsymbol{R}=2(\boldsymbol{r}_1-vt\boldsymbol{u_y})}. \tag{7}$$

The following part of the calculation involves some straightforward vectorial analysis which results in

$$\mathrm{d}N = \frac{m^2v^2}{2D^2}\mathrm{d}S\int_{k_\rho}^{\infty}\frac{|\hat{\Phi}(k,\theta,\phi)|^2}{k(k^2-k_\rho^2)^{1/2}}\mathrm{d}k. \tag{8}$$

Noting that $|\hat{\Phi}(k,\theta,\phi)|^2$ is nothing but the probability distribution $\mathcal{P}_{v,N,M_N}(k,\theta)$ of the vector $\boldsymbol{k}$ (the azimuthal angle being discarded due to cylindrical symmetry around the laser polarization vector, in the present case of linear polarization) and rewriting the prefactor dSm^2v^2/D^2 as $d^2\boldsymbol{k_\rho}$, one gets the probability $P(k_\rho,\alpha)$ to record a deuterium atom with a kinetic momentum k_ρ, on the surface element dS (pixel M) located at (ρ,α) on the CCD camera as

$$P_{v,N,M_N}(k_\rho,\alpha) = \frac{\mathrm{d}N(k_\rho,\alpha)}{\mathrm{d}^2k_\rho} = \frac{1}{2}\int_{k_\rho}^{\infty}\frac{\mathcal{P}_{v,N,M_N}(k,\theta)}{k(k^2-k_\rho^2)^{1/2}}\mathrm{d}k. \tag{9}$$

Equation (9) is precisely the Abel transformation [18], despite the fact that the experimental situation we are describing is not amenable to a simple mapping on the detector plane of a photodissociation that had already occurred in the center-of-mass frame.

The second step to reach the experimental spectra consists in an averaging over the initial rovibrational populations. Averages over M_N, N, and v are carried out successively:

$$P(k_\rho,\alpha) = \frac{1}{Q}\sum_v\frac{a_v}{Q_v}\sum_N b_N g_N\frac{1}{2N+1}\sum_{M_N=0}^{N}c_{M_N}P_{v,N,M_N}(k_\rho,\alpha). \tag{10}$$

The total Hamiltonian being invariant with respect to the sign of M_N, $c_0=1$ and $c_{M_N}=2$ (for $M_N\neq 0$). g_N takes into account the nuclear spin statistics and results for D_2^+ in

$$g_N = \begin{cases} 2 \text{ for even } N, \\ 1 \text{ for odd } N. \end{cases} \tag{11}$$

Rotational populations are thermally weighted; their Boltzman distribution is accounted for by b_N:

$$b_N = \exp\left[-\frac{\Delta E(v,N)}{k_B T_v}\right]. \tag{12}$$

$\Delta E(v,N)$ is the rotational energy, k_B the Boltzmann constant, and T_v the temperature. Finally a_v's are the initial vibrational populations resulting from the electric discharge acting over D_2. The rotational temperature T_v, as well as the initial vibrational distribution a_v is provided by experimental measurements. The normalization factors in Eq. (10) are

$$Q_v = \sum_N b_N g_N, \tag{13a}$$

$$Q = \sum_v a_v. \tag{13b}$$

The third step concerns the laser spatial intensity averaging. Although particular attention is devoted in the experimental measurements for obtaining well-focused ion beams, the molecules actually experience different field amplitudes according to their positions (y,z) due to a nonhomogeneous intensity distribution $I(y,z)$ in the laser beam. We have already observed the basic importance such an averaging has, when attempting a quantitative interpretation of H_2^+ experimental data [14]. D_2^+ photodissociation may require even wider intensity distributions as being twice slower than H_2^+ when accelerated by the same potential. It is clear that the laser intensity variation effect can be merely neglected in its propagation direction Ox, the focal volume in this direction being of the order of 1 cm as compared to the dimension of the molecular beam (200 μm). Concerning the two other directions, there is complete overlapping between the laser and molecular beam along Oy, implying the necessity of an averaging. The situation is less critical along Oz where the dimension of the beam $2L=50$ μm is of the same order than the focal area, but should be taken into account through a double spatial integration:

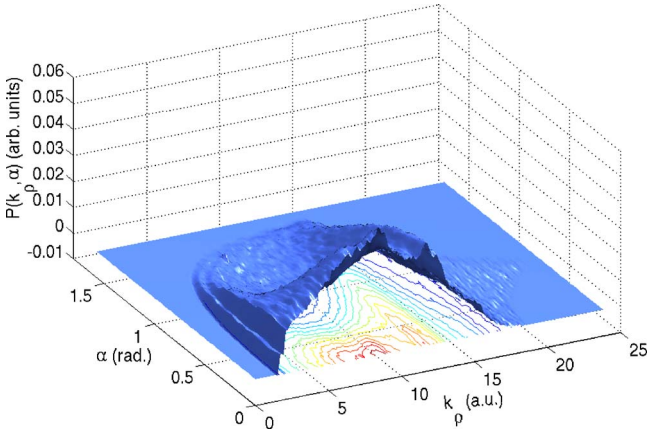

FIG. 2. (Color online) Two-dimensional experimental photodissociation image of D_2^+ using a 784.5-nm laser pulse of duration 140 fs and peak intensity of 1.5 10^{14} W/cm^2.

$$P(k_\rho,\alpha) = \int_{-L}^{L} \mathrm{d}z \int_{-\infty}^{+\infty} P(k_\rho,\alpha;I(y,z))\mathrm{d}y, \qquad (14)$$

where $P(k_\rho,\alpha;I(y,z))$ is the signal detected when the calculation through Eq. (9) is conducted for an intensity $I(y,z)$. $P(k_\rho,\alpha)k_\rho \mathrm{d}k_\rho \mathrm{d}\alpha$ is the number of dissociated molecules with momentum k_ρ (within an interval $\mathrm{d}k_\rho$) and angle α (within an interval $\mathrm{d}\alpha$) measured in terms of a fraction of surface perpendicular to the laser beam. More precisely, when multiplying this quantity by the density of particules in the molecular beam times the extension of the beam in its x direction, we get the number of dissociated molecules with k_ρ and α. A Gaussian shape is assumed for the two-dimensional behavior of the laser within the focus area with the relevant parameters obtained from the experimental setup.

The final step for building the experimental observable is the convolution with the detector resolution window taken as a square gate of 0.07 a.u. in the kinetic momentum, approximatively corresponding to a pixel size of 70 μm.

IV. RESULTS

The two-dimensional experimental image is displayed in Fig. 2, as obtained using a 784.5-nm wavelength laser pulse of 140 fs duration, carrying a total energy of 1.15 mJ. The diameter of a laser beam is measured as 110 μm, and the peak intensity is about 1.5×10^{14} W/cm^2.

The potential energy curves for the two BO states $^2\Sigma_g^+$ and $^2\Sigma_g^+$, as well as the transition dipole moment between them, have been taken from previous work on H_2^+, where they were obtained by the numerical solution of the Schrödinger equation in spherical coordinates within the range $0<R<200$ a.u. [14,19–21]. Figure 3 illustrates a diabatic view of the single- and three-photon dressed potential curves, together with the vibrational levels of D_2^+ and some of H_2^+, for comparison. The network of BO potential energy curves is of course common to H_2^+ and its isotope D_2^+, but due to its higher mass, D_2^+ vibrational levels are much denser than those of H_2^+. The single-photon curve crossing occurs between $v=12$ and $v=13$ right turning points (instead of $v=8$ and $v=9$, for H_2^+), as for the three-photon crossing it is close to the one of $v=4$ (instead of $v=2$ and $v=3$, for H_2^+). It is also worthwhile noting that the lowest vibrational level that can dissociate by absorbing a single photon is $v=7$. $v=6$, which is below the single-photon dissociation threshold, requires at least two photons to dissociate.

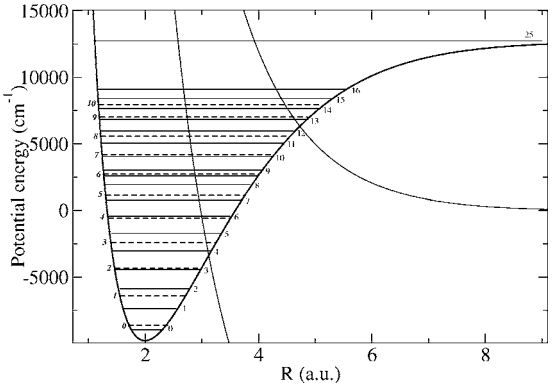

FIG. 3. Single- and three-photon dressed BO potential energy curves of D_2^+. The thin horizontal lines indicate the vibrational levels of D_2^+, whereas the dashed horizontal lines are for the vibrational levels of H_2^+.

The initial field-free vibrational populations of the parent ion D_2^+ are estimated from similar discharge experiments [22]. They are collected in terms of histograms a_v for levels $v=0$ up to 15 in Fig. 4. As in the case of H_2^+, they are subjected to errors within 10%–15% in relative values. This gives rise to a possible fit which is also indicated in Fig. 4. Another parameter, which is modified to get a better experiment-theory comparison, is the laser peak intensity which strongly depends on several experimentally measured parameters. As in our previous work on H_2^+, this adjustment has only been performed for one-dimensional spectra corresponding to cuts at $\alpha=0$, and the value of 3×10^{13} W/cm^2 has been retained.

The spectra are presented following cuts, either for fixed values of α as a function of k_ρ (yielding fragments kinetic energy distributions) or for fixed values of k_ρ as a function of α (yielding fragments angular distributions).

A. Fragment kinetic energy distributions

Figure 5 depicts the experimental and calculated spectra following a cut at $\alpha=0$. The positions of single- and two-photon dressed vibrational levels are also indicated. Although not adequately shifted by the strong radiative coupling, these indications help in understanding some features of the peak structure. The experimental spectrum shows a peak at $k_\rho\simeq10$ a.u. which corresponds to the single-photon curve crossing energy ($v=12$). But it turns out that this is not the major peak, which is actually positioned at $k_\rho\simeq7$ a.u.($v=9$). Two reasons may be invoked for explaining this fact: the initial vibrational population, as is seen from Fig. 4, clearly favors $v=9$ as compared to $v=12$ (by a factor of 3), on the one hand, and the peculiarity of the angular distributions, on the other hand. More explicitly, the dissociation at $k_\rho\simeq10$ a.u. ($v=12$, at the curve crossing region) is

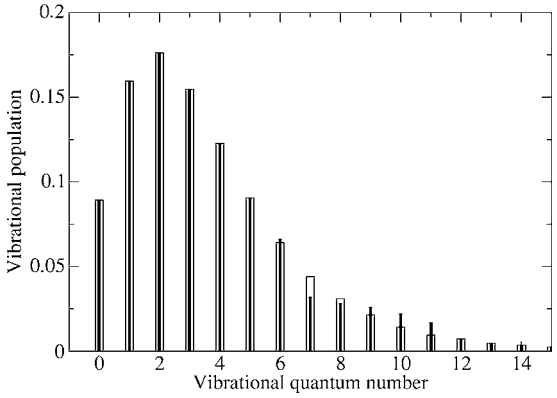

FIG. 4. Vibrational levels populations as experimentally estimated and fitted in the present work (rectangles).

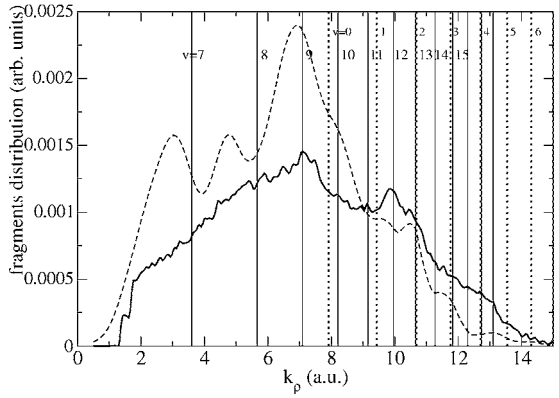

FIG. 5. Fragment kinetic energy distributions (cut at $\alpha=0$) resulting from one- and two-photon dissociation of D_2^+ (solid line for the experimental and dashed line for the calculated spectra, respectively). The vertical lines correspond to fragments momenta originated from the one- (solid line) and two- (dotted line) photon dressed vibrational levels.

very efficient (as occurs above the adiabatic energy barrier) but without a privileged direction α, whereas fragments with $k_\rho \simeq 7$ a.u. ($v=9$, below the curve crossing energy) dissociate less, but in the privileged direction $\alpha=0$, due to the bond softening mechanism which operates below the adiabatic energy barrier [23,24]. Finally a cut at $\alpha=0$ relatively enhances the contribution of fragments with $k_\rho < 10$ a.u. Fragments with higher kinetic momenta ($k_\rho > 10$ a.u.) have a rapidly decreasing probability distribution, basically due to the fact that they originate from vibrational levels ($v>12$) of the parent ion D_2^+ that are partially trapped (vibrational trapping mechanism [10,11]) at least in the $\alpha=0$ direction. The spectrum shows, as expected, a cutoff at $k_\rho \simeq 1.4$ a.u. (corresponding to $v=7$). The calculated spectrum is disappointing. The peak at the curve-crossing position $k_\rho \simeq 10$ a.u. is clearly reproduced but the lower-kinetic-momenta region ($k_\rho < 10$ a.u.) is overestimated with a three-peak structure based on $v=9,8,7$ initial levels (a somehow plausible result, although not in agreement with the experiment). An additional question is the contribution to the spectrum of the multiphoton process as in the $k_\rho > 7$ a.u. region. Such processes originate from two-photon absorptions affecting $v=0,\ldots5$ vibrational levels of D_2^+ (see Fig. 5). A calculation done by artificially putting the initial vibrational populations of $v=0,\ldots,5$ to zero, instead of their values displayed in Fig. 4, results in the single-photon contribution to the spectrum. For comparison, the full theoretical spectrum and its single-photon contribution are displayed in Fig. 6. The differences do not exceed 15% in relative values.

A fundamental reason for the unsuccessful outcome of the calculations at $\alpha=0$ can be related to the fact that the theoretical model does not account for the Coulomb explosion, which precisely occurs for angles α close to zero, corresponding to the strongest radiative interaction. Actually, the experimental spectra show that the Coulomb explosion spot is roughly limited within an angular dispersion of about $\alpha \leqslant \pi/6$ [26]. Fortunately, for angles α slightly above $\pi/6$, there is still noticeable amount of dissociation and this peculiarity can be exploited for a quantitative experiment versus theory comparison. This requires, however, a proper normalization of the fragment distributions, taking into account the part of the fragments originating from the Coulomb explosion. At high intensities D_2^+ actually dissociates through two competing channels:

$$D_2^+ \rightarrow \begin{cases} D + D^+ & \text{(channel 1, multiphoton dissociation)}, \\ D^+ + D^+ + e^- & \text{(channel 2, Coulomb explosion)}. \end{cases}$$

The experimental setup is such that only neutral species being detected, the high-energy ionic fragments of channel 2 are not directly observed. They only play a role in the total fragments versus parent ions populations, which can be formulated as

$$P_D + P_C + P_B = \mathcal{N}, \tag{15}$$

where P_D and P_C are the total (i.e., energy- and angle-integrated) fragmentation probabilities through channel 1 or 2, respectively, and $\mathcal{N}$ is the total number of molecules per unit surface perpendicular to the laser beam. P_B refers to the probability that the parent ion D_2^+ remains bound. The theoretical counterpart of Eq. (15) is nothing but

$$\tilde{P}_D + \tilde{P}_B = \mathcal{N}, \tag{16}$$

as channel 2 is not taken into account at this level of the model. A direct comparison of the differential probabilities

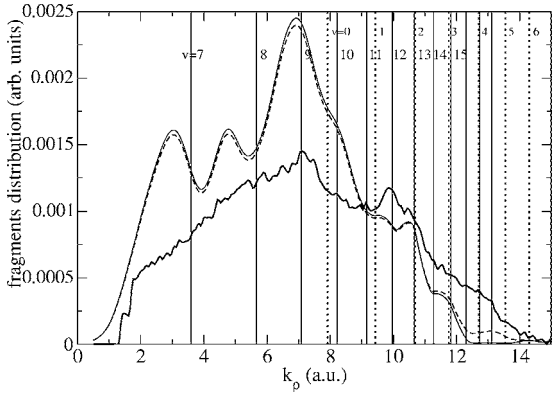

FIG. 6. Same as for Fig. 5, the additional (dotted) curve being the single-photon contribution to the calculated spectrum

$P_D(k_\rho,\alpha)$ and $\tilde{P}_D(k_\rho,\alpha)$, such as the one displayed in Figs. 5 and 6, may not be appropriate at least for some cuts in α involving strong radiative couplings responsible for Coulomb explosion. The known fact that Coulomb explosion basically occurs at relatively large interatomic distances [25] helps in disentangling the direct dissociation from the dissociative-ionization process. We assume that rotational dynamics takes part during the early steps of dissociation and is inhibited at large R (due to R^{-2} in the rotational kinetic energy). In other words, the angular distributions do not change during the Coulomb explosion process. Parent molecules exhibiting an angle α larger than α_0 (to be later determined), at distances close to the Coulomb explosion possible occurrence, actually do not experience strong enough radiative coupling to ionize. We claim that their multiphoton dissociation can adequately be described by $\tilde{P}_D(k_\rho,\alpha>\alpha_0)$. We support this claim by a numerical evaluation of the Coulomb explosion (dissociative ionization) to a pure neutral dissociating branching ratio. This is done by splitting the dissociation probability into two regions, separated by $\alpha=\alpha_0$:

$$P_D=\int_0^{k_\rho^{\max}} k_\rho \mathrm{d}k_\rho \int_0^{2\pi} [P_D^{\alpha_0<}(k_\rho,\alpha)+P_D^{\alpha_0>}(k_\rho,\alpha)]\mathrm{d}\alpha, \tag{17}$$

with

$$P_D^{\alpha_0<}(k_\rho,\alpha)=\begin{cases} P_D(k_\rho,\alpha), & \text{if } \alpha\leqslant\alpha_0,\\ 0, & \text{if } \alpha>\alpha_0,\end{cases} \tag{18a}$$

$$P_D^{\alpha_0>}(k_\rho,\alpha)=\begin{cases} 0, & \text{if } \alpha<\alpha_0,\\ P_D(k_\rho,\alpha), & \text{if } \alpha\geqslant\alpha_0,\end{cases} \tag{18b}$$

$k_\rho^{\max}$ being the largest kinetic momentum experimentally recorded (i.e., $k_\rho^{\max}=15$ a.u.). We note again that D^+ fragments originating from Coulomb explosion (not detected) would exhibit much higher kinetic energies. The appropriately normalized differential probabilities are [from Eq. (15)]

$$\mathcal{P}_D=\frac{P_D(k_\rho,\alpha)}{\mathcal{N}-P_C-P_B}, \tag{19}$$

with a theoretical counterpart given by [from Eq. (16)]

$$\tilde{\mathcal{P}}_D=\frac{\tilde{P}_D(k_\rho,\alpha)}{\mathcal{N}-\tilde{P}_B}=\frac{\tilde{P}_D(k_\rho,\alpha)}{\mathcal{N}-P_B}, \tag{20}$$

while noting that $\tilde{P}_B=P_B$ [this justifies the *a priori* use of the same $\mathcal{N}$ on the right-hand side of Eqs. (15) and (16)]. This is a consequence of the fact that Coulomb explosion only occurs during late dynamics, when the parent ion is in route for dissociation, thus without effect on the remaining bound population of D_2^+. The normalized total dissociation probability which the theory overestimates, as actually part of it is due to Coulomb explosion within the angular interval $0<\alpha<\alpha_0$, is

$$\Delta=\int_0^{k_\rho^{\max}} k_\rho \mathrm{d}k_\rho \int_0^{\alpha_0} [\tilde{\mathcal{P}}_D(k_\rho,\alpha)-\mathcal{P}_D(k_\rho,\alpha)]\mathrm{d}\alpha. \tag{21}$$

By combining Eqs. (19) and (20) together with our claim that $\tilde{P}_D^{\alpha_0>}$ integrated over k_ρ and α is a quantitative estimation of $P_D^{\alpha_0>}$, we obtain

$$\Delta(\mathcal{N}-P_C-P_B)-P_C\tilde{\mathcal{P}}_D^{\alpha_0>}=0. \tag{22}$$

Now, defining the branching ratio between the Coulomb and the pure dissociation channels as

$$\mathcal{R}_c=\frac{P_C}{P_D}=\frac{P_C}{\mathcal{N}-P_C-P_B}, \tag{23}$$

one finally gets

$$\mathcal{R}_c=\frac{\Delta}{\tilde{\mathcal{P}}_D^{\alpha_0>}}, \tag{24}$$

where Δ is given by Eq. (21), whereas $\tilde{\mathcal{P}}_D^{\alpha_0>}$ is nothing but

$$\tilde{\mathcal{P}}_D^{\alpha_0>}=\int_0^{k_\rho^{\max}} k_\rho \mathrm{d}k_\rho \int_{\alpha_0}^{2\pi} [\tilde{\mathcal{P}}_D(k_\rho,\alpha)]\mathrm{d}\alpha. \tag{25}$$

Figure 7 illustrates the variations of Δ, $\tilde{\mathcal{P}}_D^{\alpha_0>}$, and $\mathcal{R}_c$ as a function of α_0. The main observation is that the Coulomb branching ratio $\mathcal{R}_c$ remains within 10% and varies rather slowly with α_0. The Coulomb explosion channel is basically inhibited (less than 8%) for angles $\alpha_0>\pi/7$. The maximum experiment-theory discrepancy Δ is obtained for α_0 about $\pi/8$. This suggests that our model has the potentiality to accurately reproduce the experimental data for angles α exceeding $\pi/7$. For smaller angles, even if the total probability P_C for Coulomb explosion remains small as compared with the total probability P_D for dissociation, the differential spectra (i.e., energetically and angularly resolved) may significantly differ between theory and experiment as is the situation displayed in Fig. 6 for $\alpha=0$. As has already been stated, differential probabilities that can accurately be compared are $P_D(k_\rho,\alpha)$ and $\tilde{P}_D(k_\rho,\alpha)$ for $\alpha>\pi/7$ as extracted from [Eqs. (19), (20), and (23)]

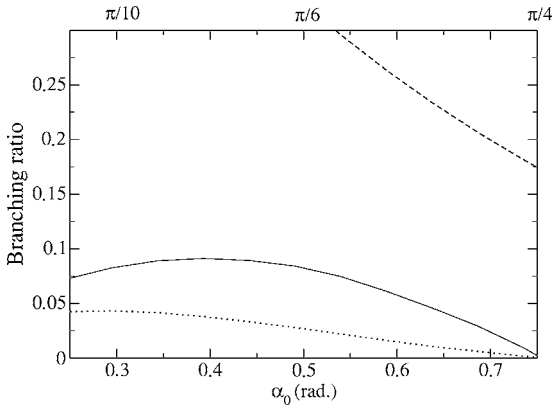

FIG. 7. Coulomb explosion branching ratio $\mathcal{R}_c$ as a function of α_0 (solid line). Are also displayed Δ (dotted line) and $\mathcal{P}_D^{\alpha_0>}$ (dashed line). See text for the notations.

$$P_D(k_\rho,\alpha) = (\mathcal{N} - P_C - P_B)\mathcal{P}_D(k_\rho,\alpha) = \frac{\mathcal{N}-P_B}{1+\mathcal{R}_c}\mathcal{P}_D(k_\rho,\alpha), \tag{26}$$

$$\tilde{P}_D(k_\rho,\alpha) = (\mathcal{N} - P_B)\tilde{\mathcal{P}}_D(k_\rho,\alpha). \tag{27}$$

The largest value of $\mathcal{R}_c$ (for $\alpha_0=\pi/7$) not exceeding 0.085 (see Fig. 7), $1/(1+\mathcal{R}_c)$, remains close to 1 and P_D differs from $\mathcal{P}_D$ only by a scaling factor $(\mathcal{N}-P_B)$. The resulting experiment-versus-theory comparison for dissociation (neglecting the Coulomb explosion) is illustrated in Fig. 8 for

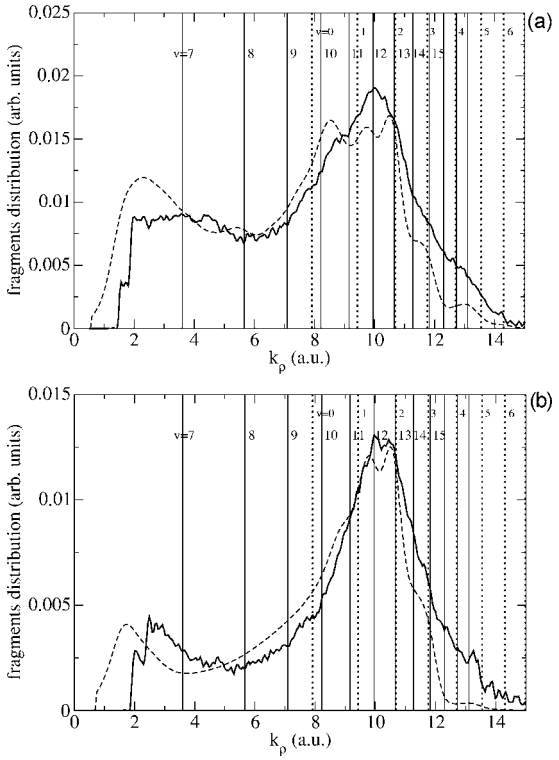

FIG. 8. Same as for Fig. 5, but for cuts $\alpha=\pi/7$ (a) and $\alpha=\pi/4$ (b).

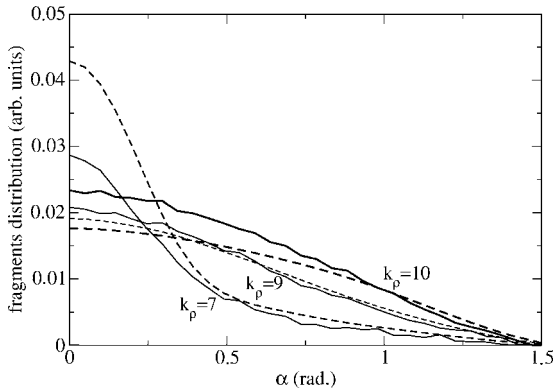

FIG. 9. Fragments angular distributions resulting from single-photon dissociation of D_2^+ for cuts corresponding to $k_\rho=7$, 9, and 10 (solid line for the experimental and dashed line for the calculated spectra, respectively).

two different cuts for angles above $\pi/7$ (i.e., $\alpha=\pi/7$ and $\alpha=\pi/4$). An excellent agreement is obtained, with the major peak close to $k_\rho \simeq 10$ a.u.

B. Fragment angular distributions

In this section, we will separately consider the alignment characteristics of fragments originating from multiphoton dissociation of D_2^+ within an experiment-theory confrontation frame and the theoretical angular behavior of fragments resulting from the absorption of two photons only (without any experimental counterpart as they cannot be disentangled from the full process). Figure 9 collects angular distributions for three cuts along kinetic momenta corresponding to fragments kinetic energies, less than the single curve-crossing energy (i.e., $k_\rho=7$ a.u.), very close to this energy (i.e., $k_\rho=9$ a.u.), and above it (i.e., $k_\rho=11$ a.u.). Fragments detected at $k_\rho=7$ a.u. (approximately originating from $v=8$) are dissociated through the bond-softening mechanism, as their energy is well below the top of the adiabatic barrier. As a consequence they are well aligned. Fragments at $k_\rho=9$ a.u. ($v=11,12$) close to the top of the adiabatic barrier are less sensitive to the bond-softening mechanism and are less aligned. Finally, fragments at $k_\rho=11$ a.u. ($v=13,14$) above the curve-crossing energy are subjected to a vibrational trapping mechanism, leading to misaligned geometries [23,24]. A good experiment-theory agreement is obtained (except for low values of α corresponding to Coulomb explosion) and the above interpretation nicely fits the tendencies of the observed distributions.

Angular distributions resulting from only two-photon absorption processes are not experimentally directly and accurately reachable. Actually, a cut at $k_\rho=11$ a.u. is the sum of contributions coming from one-photon ($v=13,14$) and two-photon ($v=2$) processes (see Fig. 5). In order to understand their mechanisms, they can, however, be calculated for a given initial vibrational level that, for energy reasons, can only dissociate after absorption of at least two photons. $v=4$ level of D_2^+ (below one-photon dissociation threshold) is such a state. Figure 10 gives angular distributions of the fragments originating from $v=4$ and calculated for different

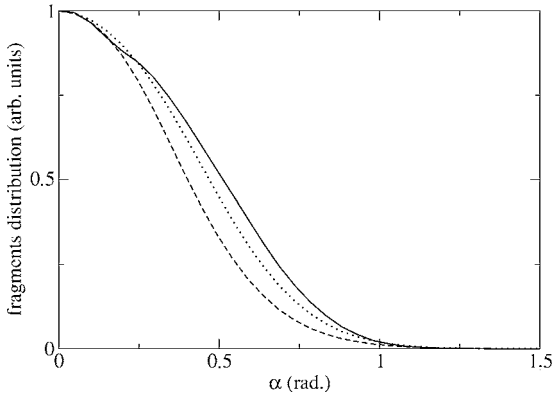

FIG. 10. Angular distributions for fragments resulting from two-photon dissociation of D_2^+ ($v=4$), for different intensities. The solid line for $I=3\times10^{13}$ W/cm^2, the dotted line for $I=5\times10^{13}$ W/cm^2, and the dashed line for $I=7\times10^{13}$ W/cm^2.

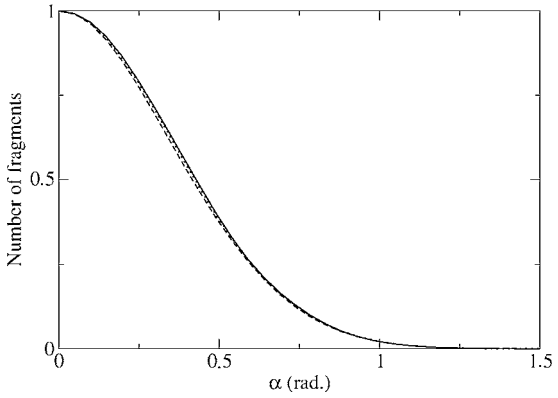

FIG. 11. Same as for Fig. 10, but for H_2^+ ($v=3$).

intensities. In general the alignment is less pronounced than in the case of single-photon dissociation. This is the consequence of the three-photon (nonadiabatic jump to the $^2\Sigma_u^+$ state) followed by one-photon emission (nonadiabatic transition to the $^2\Sigma_u^+$) processes, both misaligning [23,24]. It is only for the strong fields (10^{14} W/cm^2) that good alignment is obtained due to the bond-softening mechanism that operates at such intensities by the three-photon adiabatic barrier lowering at the curve-crossing region between the $^2\Sigma_u^+$ and and the three-photon dressed $^2\Sigma_u^+$ states. For a comparative view, we also present some two-photon dissociation alignment properties of H_2^+. Figure 11 gives the angular distribution of fragments resulting from the dissociation of H_2^+ ($v=3$) (close in energy to $D_2^+ v=4$; see Fig. 3). Here, again, we observe that alignment is less sensitive to two-photon excitations than to single-photon ones (comparing to Fig. 11 of Ref. [14]). The general intensity dependence behavior is comparable to that of D_2^+, a better alignment being, however, reached for H fragments. This is presumably due to the lighter mass that allows H fragments to better skirt around the adiabatic bond-softening barrier.

V. CONCLUSION

An experimental setup preparing the parent ions D_2^+ by electric discharge and accurate detection, yielding angularly resolved fragments dissociation spectra, provides the basis for a quantitative experiment-versus-theory comparison in strong-field multiphoton fragmentation. The quantum model, which does not account for ionization-dissociation competition, is convenient when describing the preparation step. Moreover, although Coulomb explosion plays a part for very strong fields, there are still large extent angular regions (avoiding $\alpha<\pi/7$), where the model can be safely applied. We have shown in this work that even for field strengths exceeding the ones previously used for H_2^+, an excellent agreement can be reached between experimental and calculated spectra incorporating the single- and two-photon absorption processes induced by the high laser intensities.

As of our knowledge this is one of the very first attempts to work out a quantitative bridge between experimental observables and time-dependent quantum models dealing in the molecular frame for describing multiphoton dissociation of D_2^+ irradiated by very intense, short laser pulses. A thorough understanding of the role of the relevant experimental parameters, together with a complete interpretation in terms of basic mechanisms (i.e., bond softening, vibrational trapping, nonadiabatic transition), is provided. The next challenging step would be the incorporation in the quantum model of the strong-field ionization-dissociation competition processes for a quantitative computation of the experimentally observed Coulomb explosion [15], which has, to date, found only a qualitative interpretation by the charge-resonance-enhanced ionization CREI theory [25].

ACKNOWLEDGMENT

We acknowledge computation time from Institut du Développement et des Ressources en Informatique Scientifique (IDRIS, CNRS).

[1] J. D. Buck, D. H. Parker, and D. W. Chandler, J. Phys. Chem. **92**, 3701 (1988).
[2] J. W. J. Verschuur, L. D. Noordam, and H. B. van Linden van den Heuvell, Phys. Rev. A **40**, 4383 (1989).
[3] A. Zavriyev, P. H. Bucksbaum, H. G. Muller, and D. W. Schumacher, Phys. Rev. A **42**, 5500 (1990).
[4] P. H. Bucksbaum, A. Zavriyev, H. G. Muller, and D. W. Schumacher, Phys. Rev. Lett. **64**, 1883 (1990).
[5] T. D. G. Walsh, F. A. Ilkov, S. L. Chin, F. Châteauneuf, T. T. Nguyen-Dang, S. Chelkowski, A. D. Bandrauk, and O. Atabek, Phys. Rev. A **58**, 3922 (1998).
[6] L. J. Frasinski, J. H. Posthumus, J. Plumridge, K. Codling, P. F. Taday, and A. J. Langley, Phys. Rev. Lett. **83**, 3625 (1999).
[7] D. W. Chandler, D. W. Neyer, and A. J. Heck, Proc. SPIE

3271, 104 (1998); F. Rosca-Pruna, E. Springate, H. L. Offerhaus, M. Krishnamurthy, N. Farid, C. Nicole, and M. J. J. Vrakking, J. Phys. B **34**, 4919 (2001).

[8] A. D. Bandrauk and M. L. Sink, J. Chem. Phys. **74**, 1110 (1981).

[9] A. Giusti-Suzor, X. He, O. Atabek, and F. H. Mies, Phys. Rev. Lett. **64**, 515 (1990); A. D. Bandrauk, E. E. Aubanel, and J. M. Gauthier, *Molecules in Laser Fields* (Dekker, New York, 1994).

[10] A. Giusti-Suzor, F. H. Mies, L. F. Dimauro, E. Charron, and B. Yang, J. Phys. B **28**, 309 (1995).

[11] E. E. Aubanel, A. Conjusteau, and A. D. Bandrauk, Phys. Rev. A **48**, R4011 (1993).

[12] P. Dietrich and P. B. Corkum, J. Chem. Phys. **97**, 3187 (1992); A. Conjusteau and A. D. Bandrauk, *ibid.* **106**, 9095 (1997).

[13] F. Châteauneuf, T. T. Nguyen Dang, N. Ouellet, and O. Atabek, J. Chem. Phys. **108**, 3974 (1998).

[14] V. N. Serov, A. Keller, O. Atabek, and N. Billy, Phys. Rev. A **68**, 053401 (2003).

[15] K. Sändig, H. Figger, and T. W. Hänsch, Phys. Rev. Lett. **85**, 4876 (2000); K. Sändig, H. Figger, Ch. Wunderlich, and T. W. Hänsch, in *Proceedings of the XIV International Conference on Laser Spectrosopy, Innsbruck, 1999*, edited by R. Blatt, J. Eschner, D. Leibfried, and F. Schmidt-Kaler (World Scientific, Singapore, 1999), p. 310; K. Sändig, H. Figger, and T. W. Hänsch, in *Multiphoton Processes*, edited by L. F. DiMauro, R. F. Freeman, and K. C. Kulander, AIP Conf. Proc. No. 525 (AIP, Melville, NY, 2000).

[16] I. D. Williams, P. McKenna, B. Srigengan, I. M. G. Johnston, W. A. Bryan, J. H. Sanderson, A. El-Zein, T. R. J. Goodworth, W. R. Newell, P. F. Taday, and A. J. Langley, J. Phys. B **33**, 2743 (2000).

[17] J. D. Dollard, Commun. Math. Phys. **12**, 193 (1969).

[18] B. J. Whitaker, *Photo-ion Imaging Techniques and Reactive Scattering, Research in Chemical Kinetics*, Vol. 1, edited by R. G. Compton and G. Hancock (Elsevier, New York, 1993), pp. 307–346.

[19] A. Carrington and R. A. Kennedy, in *Gas Phase Ion Chemistry*, edited by M. T. Bowers (Academic Press, New York, 1984), Vol. 3, p. 393.

[20] B. R. Judd, *Angular Momentum Theory for Diatomic Molecules* (Academic Press, New York, 1975).

[21] W. H. Press, B. R. Flannery, S. A. Teukolsky, and W. T. Vetterling, *Numerical Recipes* (Cambridge University Press, Cambridge, England, 1986).

[22] K. Sändig, Ph.D. thesis, Max Planck Institute of Quantum Optics, 2000.

[23] R. Numico, A. Keller, and O. Atabek, Phys. Rev. A **52**, 1298 (1995).

[24] R. Numico, A. Keller, and O. Atabek, Phys. Rev. A **57**, 2841 (1998).

[25] T. Zuo and A. D. Bandrauk, Phys. Rev. A **52**, R2511 (1995).

[26] D. Pavicic, A. Kiess, T. W. Hänsch, and H. Figger, Phys. Rev. Lett. **94**, 163002 (2005).